Preparations for future and current surveys

Undergraduate Research Thesis

Presented in Partial Fulfillment of the Requirements for Graduation with Research Distinction in Physics in the Undergraduate College of Mathematical and Physical Sciences of The Ohio State University

By

Paul Zivick

The Ohio State University

April 2015

Project Advisors: Professor Robert Perry and Dr. Paul M. Sutter

Abstract

The fields of astronomy and astrophysics routinely experience a cycle of planning the next generation of instruments, designing and building the instruments, before they finally go online and become available for science. However, unlike past cycles, the fields are currently poised for an unprecedented amount of data collection with the coming generation of instruments in the next decade, data on the scale of petabytes and greater. Such a high volume of data requires more intensive preparation, including creating automated pipelines to allow for easier examination of the data and understanding what types of surveys will bear the most fruit. This project aims to provide an initial forecast for the ability of voids to distinguish between models of modified gravity as well as introduce a new method of bright source removal from data collected in the radio wavelength regime.

The current leading cosmological model, known as Lambda Cold Dark Matter, successfully predicts many current observations, but slight inconsistencies have caused some to propose alternative theories that remove the need for dark energy. One such class of theories involves the modification of gravity to account for the observed apparent acceleration of the universe. In particular, we choose to examine a specific type of modification, known as f(R) gravity. In low density regions, this

modification results in gravity being stronger than normal General Relativity would predict. Because of this, low density regions in the universe, known as voids, would appear to be viable areas to test for the validity of this modified gravity model. We plan to use simulations modeling planned survey volumes roughly two orders of magnitude greater than current observations provide using realistic survey conditions to examine the effect of f(R) modified gravity on void properties, including void abundances, radial density profiles, radial velocity profiles, and void ellipticities.

The other branch of the project will focus on the processing of radio interferometric observations of neutral 21cm emission from the epoch of reionization, an era of the universe's history that holds much interest but relatively little progress has been made due to difficulties in observations. A common problem encountered is the presence of bright foreground objects that obscure nearby objects on the plane of the sky. For high resolution observations, current methods of data processing identify bright sources, convert the data to a low-resolution mesh due to computational constraints, fit the source with an ellipse, and subtract it out. We suggest that a more careful method is available through locally refining the bright spots using the high resolution data, avoiding the computational limitations, fitting the shape of the source, subtracting it, then de-refining the local patch to the original mesh. This will be particularly important for current instruments such as the Murchison Widefield Array and future instruments such as the Hydrogen Epoch of Reionization Array and the Square Kilometer Array.

Dedication

Dedicated to my family who have always encouraged me to pursue my passions.

Acknowledgments

I would like to thank Benjamin Wandelt, Alice Pisani, Nico Hamaus, and Florent Leclercq for their discussions and advice.

I would like to thank Baojiu Li and Tsz Yan Lam for helping me to use their simulations.

I would like to thank the OSU Department of Astronomy for organizing the Summer Undergraduate Research Program and the Center for Cosmology and Astroparticle Physics for supporting me through the summer.

I would like to thank Dr. Perry for his advice and patience with a student in his final semester.

And finally I would like to extend my greatest offering of thanks to Paul Sutter who has helped me to do more as an undergraduate than I had thought possible.

Table of Contents

List of Figures

Chapter 1: Introduction

1.1. Alternative Cosmologies

The leading cosmological model, the inflation plus cold dark matter (ΛCDM) paradigm, has successfully made predictions for observations which have been supported by observations throughout the last decade. However, the model does not directly address the properties of dark matter, the matter in the universe that appears to only interact gravitationally, preventing direct observation, nor the properties of dark energy, the name given to the energy in the universe causing the universe to accelerate in its expansion (e.g., Reid et al. 2012; Planck Collaboration 2014a). The existence of dark matter has been accepted as fact by much of the field, but the tenuous nature of dark energy continues to generate alternative explanations for the observational results. One such proposal that would remove the need for dark energy is the modification of the model of gravity. The motivation stems from the fact that gravity acts as the main interaction at large scales and accordingly has shaped the evolution of the universe, so perhaps a more accurate description of gravity could account for questions left unanswered by ΛCDM. While there are many different proposed modifications (e.g., Dvali et al. 2000; Maartens 2004)), this paper will focus on a single example from the *f(R)* class of models, which contain relatively simple modifications to GR and act as a useful tool to build a better understanding of the potential effects of modified gravity. The specifics of the model used will be discussed in Chapter 2.

A key feature of the *f(R)* model is the presence of the chameleon mechanism (Khoury and Weltman 2004). One problem frequently encountered in proposed modified gravity models is the necessity to build them so as to pass current solar system tests. However, any model that strengthens gravity will struggle to pass in overdense regions such as the solar system. That is where the chameleon

mechanism comes into effect, by coupling the gravity modifications to the local density, which in turn suppresses the effects of modified gravity in high density regions while allowing it to be unscreened in underdense regions. Past studies have tested *f(R)* models for different observational signatures, from the degree of curvature in superclusters (Shim et al. 2014), which found that superclusters tended to be straighter in ΛCDM, to galaxy population statistics (Fontanot et al. 2013), which found that there was no significant difference between ΛCDM and *f(R)*, to the ISW effect on the power spectrum (Cai et al. 2014), which found potentially detectable differences between the models in both the linear and nonlinear regime. Between these studies and current observations, an upper limit on the strength of modified gravity does exist, and this paper examines only strengths that are currently allowable.

1.2. Voids as Cosmological Probes

While previous works have focused on attempting to test *f(R)* gravity in high density regions, perhaps a more natural choice for examination would be the underdense regions as the modified gravity would be unscreened there. These underdense regions, commonly referred to as voids, could then provide a potentially more dramatic means of distinguishing between ΛCDM cosmology and modified gravity models than probes in high density regions. Already these voids have been used as a potential diagnostic for examining other alternative cosmologies known as coupled dark energy-dark matter models (Sutter et al. 2015), and have been used in applications such as weak anti-lensing (Melchior et al. 2014; Clampitt et al. 2014), the Alcock-Paczynski test (Lavaux and Wandelt 2012; Sutter et al. 2012b, 2014), and the integrated Sachs-Wolfe effect (Planck Collaboration 2014b; Iliić et al. 2013), demonstrating the usefulness of voids as cosmological probes. With regard to modified gravity and voids, some efforts have been made already to explore this avenue (Li et al. 2012; Clampitt et al. 2013), and initial results provide hints that voids may indeed be a viable testbed.

One obstacle in using voids as probes lies in the number of voids available to examine in observations. As they are defined by the absence of matter, the

number of voids is severely outnumbered by the number of tracers used to identify voids, such as galaxies. For every one void, it might require dozens of galaxies to properly recognize the presence of a void, which in turns affects the strength of the statistical tests for voids. An additional consideration in the statistical tests lies in the choice of void finding algorithm, as the definition used by the algorithm will impact the sensitivity of the void properties. In recent years efforts have been made to produce larger collections of voids found through these algorithms for the scientific community to use and study. Currently available void catalogs (Pan et al. 2012; Sutter et al. 2012b, 2014) from the SDSS galaxy surveys (Abazajian et al. 2009; Ahn et al. 2012) have enabled for the first time direct comparisons of predicted void characteristics to actual survey data for low redshifts. And current void-based studies of modified gravity have analyzed both redshift 0 conditions as well as higher redshift conditions through the use of a spherical underdensity void finding algorithm (Li et al. 2012; Cai et al. 2014). Upcoming surveys such as Euclid (Laureijs et al. 2011) and WFIRST (Spergel et al. 2013) will target higher redshifts, unlocking a tremendous number of voids (Pisani et al. 2014). It is thus necessary to provide a proper forecast of the ability of voids found through the watershed transform to distinguish modified gravity models in this new observing regime.

To this end, we present an assessment of the impact modified $f(R)$ gravity models on various void statistics, such as number functions, ellipticities, and radial density profiles. We focus on simulations modeling the higher redshifts, large volumes, and sparse densities comparable to upcoming surveys to look for observationally-viable distinguishing characteristics of the voids produced by the different models.

1.3. Interferometry

In addition to providing predictions for upcoming surveys, a second project began with the aim to provide a process for processing radio interferometric observations of 21 cm emission from the epoch reionization. Prior to this stage in the universe's history, the matter throughout the universe was neutral, meaning few photons were

produced to allow us to observe what happened during this period. Only once fluctuations in the matter distribution had begun to collapse were the first stars and galaxies produced, creating high energy photons that began to ionize the neutral matter around the objects, beginning the epoch of reionization. During this period and in the preceding time, in the high density regions of neutral hydrogen gas, it was possible for collisions between atoms to cause them to shift energy states slightly and the subsequent relaxation would produce photons of wavelength 21 cm (Iliev et al. 2002). These 21 cm lines as the rate of production is tied to the density of the hydrogen can help to provide information on the earliest structures that formed in the universe, fleshing out a period in the universe's history that remains relatively unknown.

Various projects are currently underway to attempt to provide more data and begin to answer these questions, such as the Murchison Widefield Array (MWA) (Lonsdale et al. 2009) and the Low Frequency Array (LOFAR) (van Haarlem et al. 2013). Both of these projects in turn, while currently sensitive enough to begin probing reionization, are precursors to the planned next generation of satellite arrays, the Square Kilometer Array (SKA). With data finally beginning to be collected on 21 cm emission lines, the importance in properly handling the observations has never been higher.

Unfortunately a drawback of these observations lies in their nature: they are some of the oldest things in the universe and as such, nearly everything in the universe stands between them and us. This results in various luminous objects such as galaxies and stars obscuring parts of the background field that is being observed. Two approaches have been developed to deal with these intrusive objects. The first, known as *avoidance*, discards any information that may have been contaminated by foreground noise in order to reduce the total noise in the measurements (Parsons et al. 2014). The second is a more aggressive approach, aiming to subtract areas of the sky that are contaminated in order to increase the total amount of data available to use, at the risk of introducing more noise into the calculations. This project focuses on the latter method as we attempt to create a more refined manner of removing

these foreground objects to reduce the artificial noise created in the process to help produce cleaner data.

1.4. Scope of Thesis

In Chapter 2, we discuss the specifics of the model of *f(R)* gravity used, the simulations analyzed, and the toolkit used for finding voids. In Chapter 3, we discuss the effects of modified gravity on void characteristics, followed by conclusions for voids in Chapter 4, with the implications for future surveys and potential options for more refined forecasts. Finally in Chapter 5, we present the current state of an effort to provide a more refined interferometric data processing technique with the aim to be incorporated in the automated pipeline for data reduction.

Chapter 2: Simulation and Void Finding

2.1. Modified Gravity Models

The particular class of modified gravity theories analyzed in this paper, denoted by *f(R)*, is marked by the generalization of the Ricci scalar R in the Einstein-Hilbert action. When combined with the chameleon mechanism, the structure formation equations become

$$\nabla^2\Phi = \frac{16\pi G}{3}a^2\delta\rho_M + \frac{a^2}{6}\delta R(f_R), \tag{2.1}$$

$$\nabla^2\delta f_R = -\frac{a^2}{3}[\delta R(f_R) + 8\pi G\delta\rho_M], \tag{2.2}$$

where the gravitational potential is denoted by Φ, the f_R value is the scalaron, defined as $\frac{df(R)}{dR}$, which is the extra scalar degree of freedom, δR and $\delta\rho$ are the differences between the local values and the background values, denoted as $R-\bar{R}$ and $\rho-\bar{\rho}$ respectively, with the barred quantities being the background values. Typically, the gravitational potential in general relativity (GR) depends only upon the matter distribution, $\delta\rho_M$, with G remaining constant. However, with the addition of the scalar field, Newton's constant also becomes dependent upon ρ_M. In the limit of low, underdense regions, G effectively becomes strengthened by a factor of 1/3 as the second term in Eq. (2.1), $\delta R(f_R)$, vanishes. In the opposite limit, in high density regions, δf_R in Eq. (2.2) approaches zero, which sets $\delta R(f_R) = -8\pi G\delta\rho_M$. When Eq. (2.1) is re-evaluated with this, one sees that $\nabla^2\Phi$ now matches local GR. This is how the chameleon mechanism allows $f(R)$ gravity to pass solar system tests, crucial in making sure $f(R)$ remains feasible.

To follow the full non-linear evolution, Eqs (2.1) and (2.2) cannot be solved analytically, so N-body simulations are required for analysis. For this work, we used the simulations described in Zhao et al. (2011). The model of gravity assumed for the simulations was of the form $f(R) = \alpha R/(\beta R + \gamma)$ where $\alpha = -m^2 c_1$, $\beta = c_2$, and $\gamma = -m^2$, all determined by three underlying variables. Of the three, only one is predetermined, with $m^2 = H_o^2 \Omega_M$, where H_o is the Hubble flow at present day and $Omega_M$ is the portion of the energy of the universe that is in matter form. The other two variables, c_1 and c_2, are free parameters that determine both the expansion rate of the universe in the $f(R)$ model, given by the ratio c_1/c_2, as well as the rate of structure formation, which is proportional to c_1/c_2^2. The structure formation specifically depends upon the value of $|df/dR|$ at redshift zero, referred to as $|f_{R,0}|$. To ensure a valid comparison to ΛCDM cosmology, c_1/c_2 was set equal to $6\Omega_L/\Omega_M$, which provides the same expansion history as in ΛCDMand an agreement of the value of σ_8 with GR at redshift 0, which ensures similar initial fluctuation conditions in the beginning of the universe. Similar to the role of the chameleon mechanism, these parameters are values that current observations can measure. In order to keep the models feasible, the parameters for the models must be chosen to reproduce these measurable quantities. The values chosen for $|f_{R,0}|$, 10^{-4}, 10^{-5}, 10^{-6}, pass current solar system tests. Hereafter these different models will be referred to as F4, F5, and F6, respectively.

2.2. N-body Simulations

Each model of modified gravity was simulated six times, creating six realizations for study, including GR (i.e., $|f_{R,0}| = 0$). Each simulation box contained 1024^3 dark matter particles and had a cubic volume of 1.5 h^{-1}Gpc per side. For this paper, we selected snapshots at scale factors of $a = 0.7$ and $a = 0.5$, corresponding to redshifts $z = 0.43$ and $z = 1.0$. The latter redshift represents the peak galaxy number density regime of the Euclid survey (Laureijs et al. 2011). At this redshift, the expected survey volume will exceed the simulation volume, which will help to decrease statistical errors further. The redshift $z = 0.43$ represents, under reasonable assumptions, the survey volumes for a spectroscopic ground-based mission such as DESI (Levi et al. 2013).

2.3. Void Identification

We subsample the simulation dark matter particles to a mean density of $\bar{n} = 2 \times 10^{-3}$ per cubic h^{-1}Mpc to provide a realistic tracer density in the void finding process, again to provide comparable results to future surveys. Current estimates for Euclid and DESI place the mean density of galaxies at $\bar{n} = 1.6 \times 10^{-3}$ per cubic h^{-1}Mpc and $\bar{n} = 2.6 \times 10^{-3}$ per cubic h^{-1}Mpc , respectively. As a result, our analysis will tend to underestimate signal produced by ground based surveys while slightly overestimating the potential significance in space based surveys. The impact of changes in the tracer density on voids will be further discussed in Chapter 4. In addition, particle positions were perturbed according to their peculiar velocities to demonstrate the observable properties in redshift space, negating the need to correct for redshift-space distortions. It should be noted that although this paper aims to develop an intuition for the observational indicators of modified gravity, we choose to ignore the effects of galaxy bias, as Sutter et al. (2014) demonstrated that certain void properties from catalogs compiled using a watershed based void finder are relatively insensitive to bias.

Chapter 3: Analysis of Void Properties

In our analysis of the simulations, we will examine in detail four properties: abundances, radial density profiles, radial velocity profiles, and ellipticities. Previous works have shown the susceptibility of these properties to changes in gravity (e.g., Bos et al. 2012; Sutter et al. 2015; Cai et al. 2014). This work focuses on the observational relevancy of each property, so we will present the analysis with emphasis on the strengths and weaknesses each property displays. For each property discussed below, the mean values correspond to the mean across all six realizations. We take the quoted variance to be either the cosmic variance or the intrinsic scatter, depending on which is larger, to be as pessimistic as possible. All properties were calculated using built-in functions in VIDE, with slight modifications made to accommodate handling multiple realizations.

3.1. Abundances

Figure 3.1 shows the cumulative number function from ΛCDM and the modified gravity simulations at redshift 1.0, and Figure 3.2 shows the number function at redshift 0.43. Along the x axis is the effective void radius (the radius of a sphere with the same volume as the void). On the top portion of the plot is the log of the number of voids larger than a given effective radius per cubic h^{-1}Gpc, and in the lower portion is the relative significance of the models F4, F5, and F6 compared to GR. The uncertainty plotted in the top portion is the square root of the cosmic variance. For the bottom plot, the difference between the number of voids in the GR model and in the $f(R)$ models was divided by the square root of the sum of variances from the two models. This provides a weighted indication of where the differences provide the most statistically significant signal.

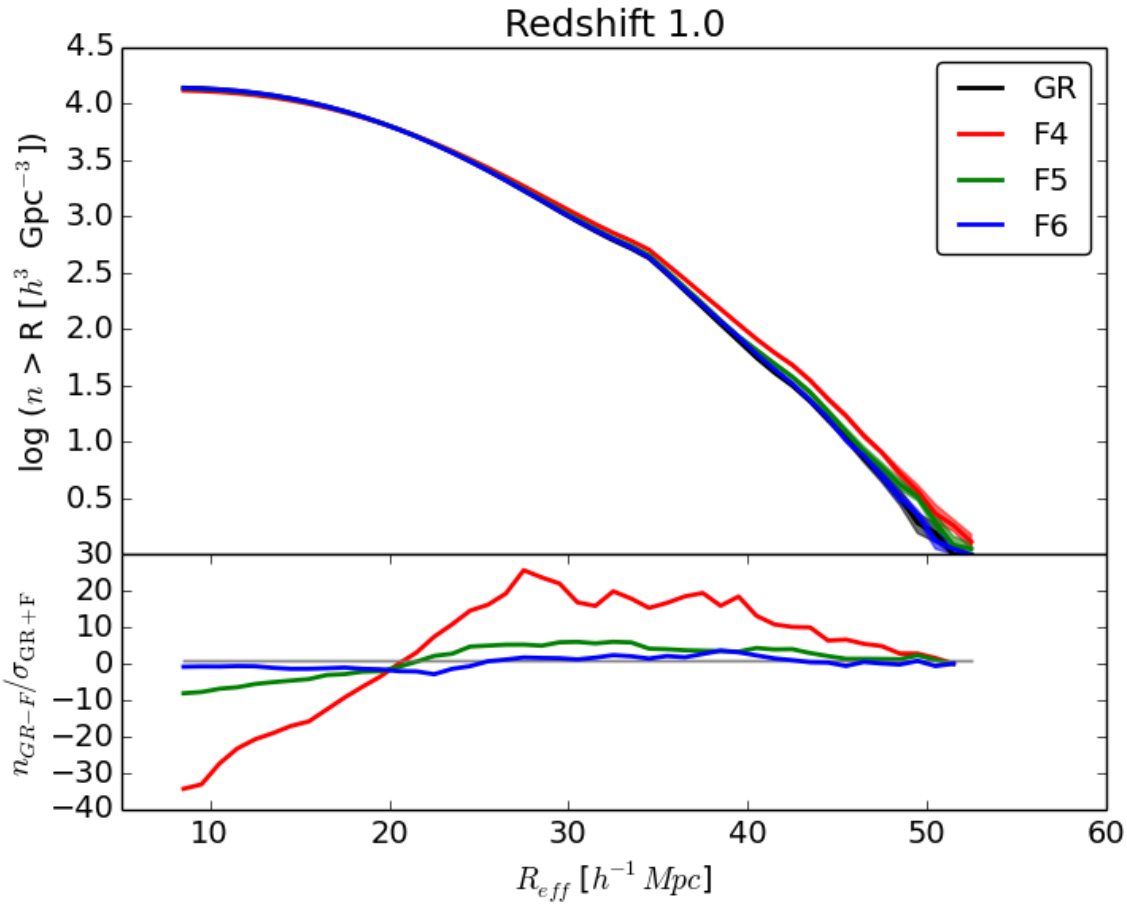

Fig. 3.1.— Cumulative void number functions. The upper panels show the abundances for General Relativity (GR; black) and modified gravity models F4 (red), F5 (green), and F6 (blue) from realistically subsampled dark matter particle simulations. The solid lines are the mean number functions of the six realizations, and the shaded regions are the 1σ cosmic variances for each mean. The lower panels show the relative significance of each model compared to GR. Larger values of $|f_{R0}|$ cause the modified gravity to turn on at earlier ages, accelerating the evacuation of matter compared to GR, leading to fewer small voids and more large voids.

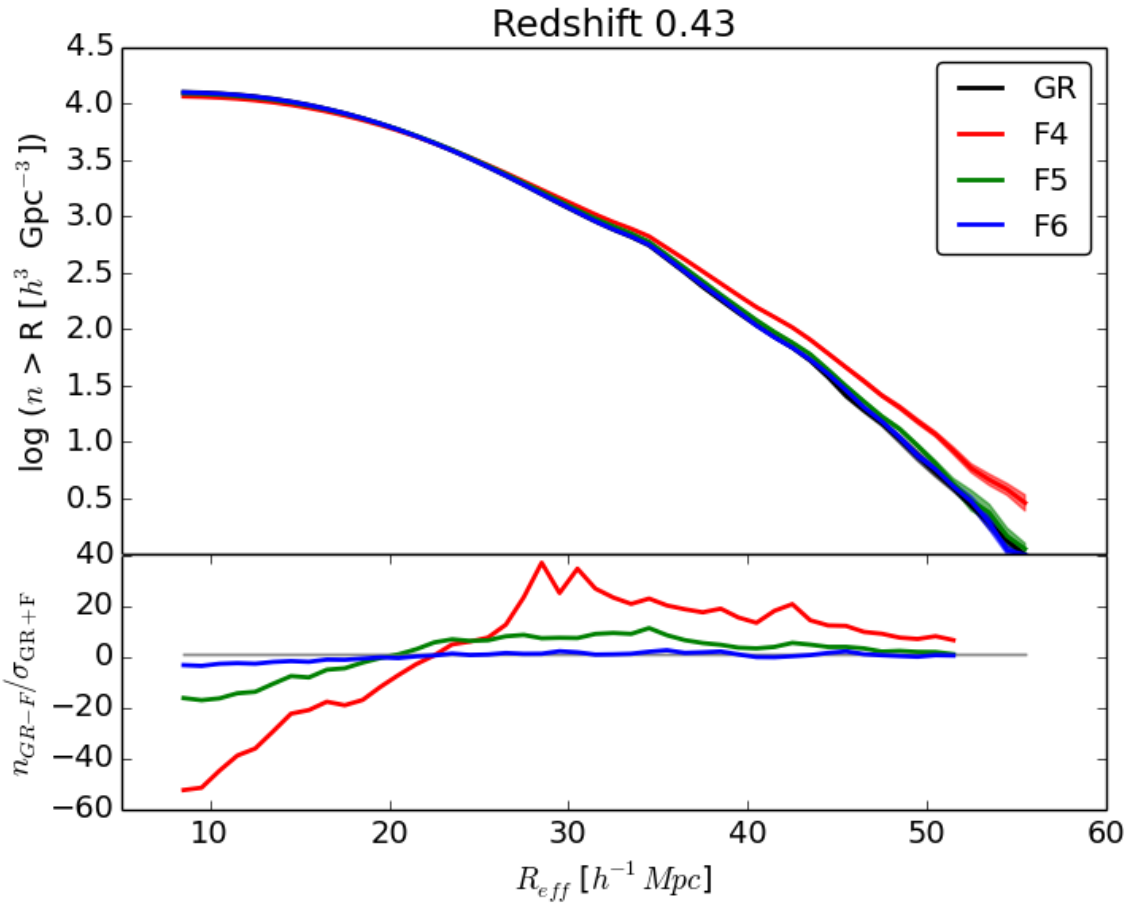

Fig. 3.2.— Cumulative void number functions. The upper panels show the abundances for General Relativity (GR; black) and modified gravity models F4 (red), F5 (green), and F6 (blue) from realistically subsampled dark matter particle simulations. The solid lines are the mean number functions of the six realizations, and the shaded regions are the 1σ cosmic variances for each mean. The lower panels show the relative significance of each model compared to GR. Larger values of $|f_{R0}|$ cause the modified gravity to turn on at earlier ages, accelerating the evacuation of matter compared to GR, leading to fewer small voids and more large voids.

We can see that F4 clearly contains larger voids than in the ΛCDM simulation at both redshifts. Even at the higher redshift, in the roughly 40 h^{-1}Mpc radius range, there are still enough voids to provide significant statistical power in distinguishing between the F4 model and GR, clearly indicated by the relative significance plots. As the effective radius continues to increase though, the significance drops off, suggesting there are only certain regimes of void size that will be suitable for diagnostics. It becomes difficult to see any clear differences between the weaker coupling strengths and GR, especially at redshift 1.0. However, due to the large numbers of voids being examined, the errors on the abundances for F5 become small enough to separate from that model from GR, most notably in two separate regimes, the small voids on the order of 10 h^{-1}Mpc and the medium-large voids on the order of 30 h^{-1}Mpc. While the differences can be detected at both redshifts, at the lower redshift, the significance, especially in smaller voids, is noticeably larger, almost by a factor of 2.

The obvious tilt in the number function reveals the effect of the modified gravity on the structure of voids: the smaller voids in GR have been emptied out and the void walls have begun to thin, allowing the watershed algorithm to merge them together, as seen in the coupled DM-DE analysis of Sutter et al. (2014). This produced few small voids and more large voids. However, despite the $\sim 20\%$ differences in the number of large voids, the peak relative significance occurs for small and medium-scale voids, where the increased statistical significance overcomes the relatively smaller absolute differences. Similarly, even though the modified gravity models produce larger absolute differences at lower redshifts, there are few overall voids, so the relative significance remains largely unchanged.

The evolution of these differences align with what one would reasonably expect to see from the $f(R)$ models. At higher redshift, the voids have not had time to empty out. Because the modified gravity from the scalar field in $f(R)$ is dependent upon the local density, until voids empty out enough, the modified gravity will remain screened, making the $f(R)$ models appear identical to GR. Simultaneously, as time progresses and observations move to lower redshifts, they see a universe that has had time to mature, one that has given the modified gravity more time to act

upon the voids, expanding them more rapidly than normal GR would, resulting in a higher overall number of large voids. The ordering that is prominently displayed in the lower redshift plots stems from the differing strengths of the modified gravity, with the strongest force, F4, producing the greatest number of large voids.

To provide an initial estimate of the ability of these voids to constrain the value of $|f_{R,0}|$, we perform a simple Fisher forecast by constructing a numerical derivative of the abundances as a function of parameter strength:

$$\Delta f = \sum_{i=1}^{N} \frac{(n_{\mathrm{F4},i} - n_{\mathrm{GR},i})^2}{10^{-4} \times \sigma^2_{F4,i}}, \tag{3.1}$$

where Δf is the resulting forecasted upper limit, $n_{\mathrm{F4},i}$ and $n_{\mathrm{GR},i}$ denote the void number density in radial bin i for the F4 and GR simulations, respectively, N is the total number of radial bins, σ^2_{F4} is the variance in a bin, and 10^{-4} is the difference in the $|f_{R0}|$ parameter value between the F4 and GR model. Using this prescription, we find that we can place an upper limit of 5.82×10^{-5} for voids at redshift 1.0 and 4.78×10^{-5} at redshift 0.43 on the value of $|f_{R,0}|$. As one might expect, with the greater differences between models at more recent times, we are able to more tightly constrain the value. With upcoming surveys, if more redshift epochs are available for analysis, the combined information may even be able to rule out F5.

3.2. Density Profiles

In Figure 3.3 we show the mean one-dimensional radial density profiles for two different radial bins, 15-20 h^{-1}Mpc and 30-35 h^{-1}Mpc (representing, respectively, over- and under-compensated voids) for the six realizations. On the bottom portion of each plot, we show the relative significance between each model. In the legend, beside each model type is the total number of voids used to calculate the mean profiles. Within each realization, we computed the profiles by selecting voids within a given radial range and aligning their volume-weighted centers. With a sufficient number of voids, the average shape of a void approaches a sphere, so the radial densities were measured by taking the number of particles within thin spherical shells. We normalized these densities to the mean number density of the realization

and plotted them against the effective radius, R/R_v, where R_v is the median void size in each stack.

It is important to note that error bars were plotted for the normalized plots, but due to the high number of voids used to calculate the profiles, the error bars are not visible.

Upon first examination, one does not notice any drastic differences in the normalized profiles between the models in either redshift. However, looking at the relative significance plots below the normalized profiles, one sees that the differences in the compensation regions are in fact significant by up to 3σ for a redshift of 0.43. The differences are most apparent in the compensation shells surrounding the voids, where changes to void histories lead to differences in the pile-up of matter surrounding them. The interiors of the voids are correspondingly emptier in the modified gravity models, with the switch between relatively over and under dense (compared to GR) appearing mid-wall. At higher redshifts, this switch occurs at higher radii for stronger gravity models, but by lower redshifts the switch occurs at nearly the same radius, since further void evolution is constrained by surrounding structures. By $\sim 2R_{\rm eff}$ the differences disappear. Similarly, at the void centers the uncertainties are so large that the relative significance approaches zero.

Similar to the abundances, there is an ordering of the models with the weaker modified gravity models being closer to GR, as expected. We see here the impacts of modified gravity on void evolution. The enhanced gravity acts on the particles within the voids, accelerating them to the edges of the voids faster than GR would, causing the interiors of the voids to be less dense compared to GR while creating a build up of particles in the walls of the voids, leading to the denser overcompensated regions. As the voids are given more time to evolve and for the modified gravity to act, these differences become even larger, as one can discern from the transition of the plots from redshift 1.0 to redshift 0.43. However, one will notice that the weakest modified gravity model F6 does not have a noticeable trend in the significance plot, instead fluctuating back and forth across the GR baseline value. This holds for all four profiles examined, with the relative significance never rising above 1σ. Even F5 struggles to differentiate itself, with its significance values only just rising above 1σ

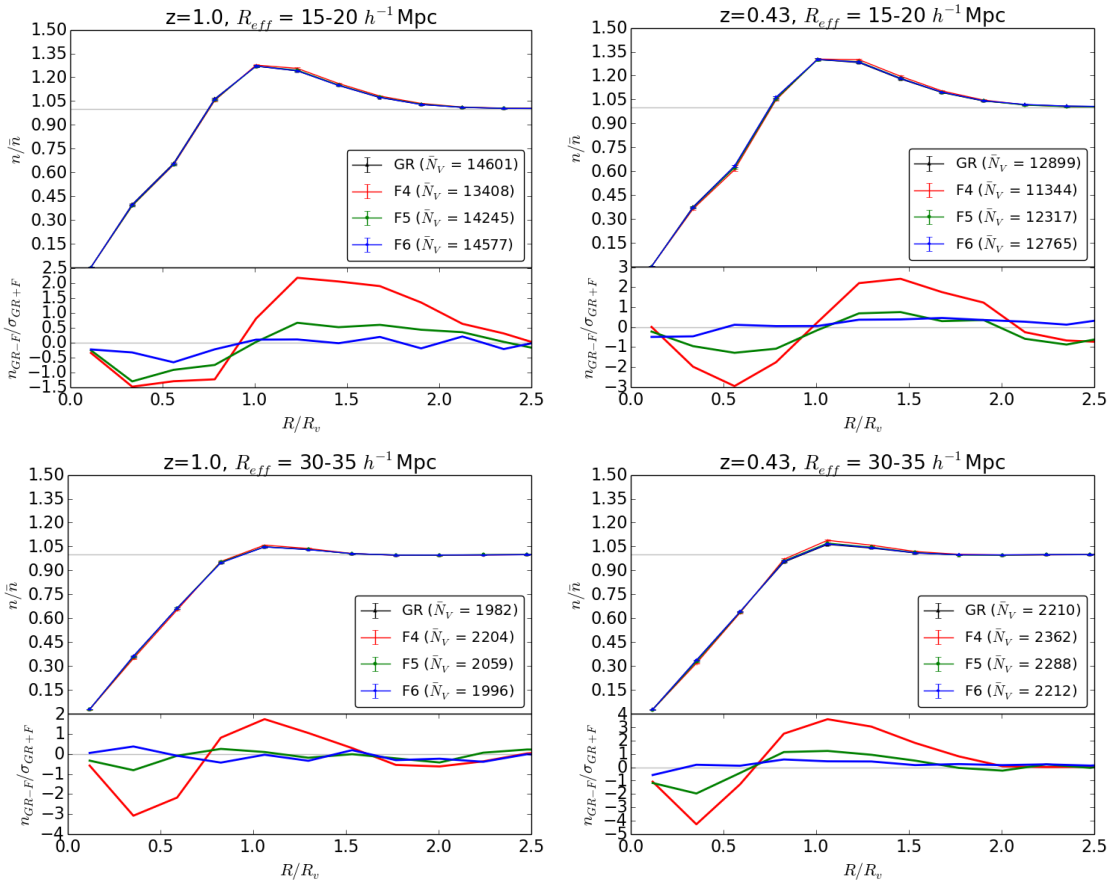

Fig. 3.3.— Mean radial density profiles of stacked voids with 1σ uncertainties (upper panels) and relative significance of the profiles compared to GR (lower panels). The legends indicate the cosmological model and mean number of voids N_v used to calculate the profiles. The thin gray lines represent mean density in the upper panels and the GR relatively profile in the lower panels. The density is plotted against the relative radius, where R_v is the median void radius in each stack. The accelerated evacuation under modified gravity generates a slightly greater build up in the compensation region, more noticeable at a lower redshifts.

for redshift 1.0. Only when the voids have had more time to evolve at redshift 0.43 are there any potentially consistently measurable differences for F5.

Despite the lower significance of these differences, void density profiles may be an appealing target for future surveys, since they can be accessed in real space in a parameter-free way (Pisani et al. 2014) and are not affected by survey masks (Sutter et al. 2014), provided that the model of gravity required is sufficiently modified.

One other potential route to extract more information from the radial density profiles is to fit them using the profile model proposed in Hamaus et al. (2014), hereafter referred as the HSW profile. This model provides a universal void profile that requires only two parameters, the central density of the voids δ_c and the scaling radius r_s. Fitting to this profile allows us to neatly summarize any systematic differences between modified gravity models and GR. We split the voids into bins by radius, going from $10-15\ h^{-1}$Mpc in steps of $5\ h^{-1}$Mpc up to $40-45\ h^{-1}$Mpc. The results of the fit can be seen in Figure 3.4. In the plots the thin gray line indicates where the voids transfer from being overcompensated to undercompensated.

While individual stacks do not provide statistically significant differences, we may discern a systematic trend: modified gravity models produce voids with lower values of both δ_c and r_s, with F4 producing the largest differences. The fits to the HSW capture the quintessential differences between the models and GR: modified gravity produces emptier, more steeply-walled voids.

To quantify the significance of these differences, we found the weighted distance between each fit using the prescription

$$d = \sqrt{\frac{(x_{GR} - x_F)^2}{\sigma_{x,GR}^2 + \sigma_{x,F}^2} + \frac{(y_{GR} - y_F)^2}{\sigma_{y,GR}^2 + \sigma_{y,F}^2}}, \tag{3.2}$$

where x refers to the r_s/R_v value, y refers to the δ_c value, F refers to the modified gravity model (as this distance was calculated for the three models, F4, F5, and F6), and σ^2 refers to the variance in the fit for the respective values. This acts as an analog to the relative significance plots from the radial densities and the abundances. Using this prescription, we find that the total significances for F4 are 1.0 and 1.8, for

F5 are 0.4 and 0.7, and for F6 are 0.3 and 0.3, for redshifts 1.0 and 0.43 respectively. While it comes as no surprise that the F6 model struggles to separate itself from GR, even under this severe compression of the data the F5 and F4 models are only mildly distinguishable from GR, showing a significance lower than the radial density profiles displayed at their peaks.

3.3. Radial Velocity Profiles

In Figure 3.5 we plot the radial velocities profiles for the same radius stacks as the density profiles. As before, the top panels show the profiles with 1σ uncertainties and the bottom plots show the relative statistical significances. Positive values indicate outflows and negative values indicate inflow relative to the void center. As expected, we see that the larger voids have much faster outflow velocities, by up to a factor of two. This is because the larger voids are not surrounded by overdense shells, and thus do not have their expansion constrained by any surrounding matter. For a similar reasons the velocities never drop below zero for the largest voids, indicating that they will continue expanding, unlike their smaller, overcompensated counterparts.

The differences between the modified gravity models and GR are visually apparent, in contrast with the density profiles. Under the influence of modified gravity, the peak outflow velocities at late times increase by up to $\sim 20\%$ in the F4 model. The corresponds to a reduced outflow outside the void for larger stacks and an enhanced inflow for smaller stacks. Since modified gravity directly affects acceleration, it is not surprisingly that velocities will be impacted more than densities. However, velocities also have considerably more scatter, so despite these strong differences, the relative significance remains similar to what we observed earlier in the radial density profiles.

The velocity profiles offer one unique advantage compared to the other void properties previously examined: a strong difference that persists at higher redshifts. Indeed, the void interiors have more significant differences at higher redshifts than at lower ones, since the growth of the voids has not yet been strongly affected by their surroundings (i.e., either by the build-up of an overdense shell or by running into

adjacent voids). The changes already present at high redshift in the velocity profiles will not manifest themselves in the density profiles or abundances until later times.

Velocities then potentially offer better leverage in the higher redshift surveys than density profiles, but it still cannot begin to match the abundances in terms of overall significance.

3.4. Ellipticity Distributions

The final void property we examine is the ellipticity, a measure of how non-spherical the shape of a void is. In Figure 3.6, histograms show the mean void ellipticity of each model, marked by the black line, and the 1σ and 2σ errors on the mean, marked by the darker gray and lighter gray areas respectively. To calculate the ellipticity we use the inertia tensor to compute eigenvalues and eigenvectors and form:

$$\epsilon = 1 - \left(\frac{J_1}{J_3}\right)^{1/4}, \tag{3.3}$$

where J_1 and J_3 are the smallest and largest eigenvalues of the inertia tensor, respectively.

Unlike the properties studied above, there is no clear ordering from the strongest coupling strengths to the weakest coupling strengths. The notable outlier is the strongest coupling strength, F4, which is a few σ removed from the means of the other models. However, aside from this outlier, there is no readily discernible pattern to be seen. For the higher redshift, none of the calculated mean ellipticities appear to be statistically significant from each other, suggesting an overall similar shape to the voids at this point in the universe's evolution. At a later time, the voids have evolved further to begin to have a set shape in the universal environment, but there is no apparent pattern in how the mean ellipticities are chosen for each model, as the weakest model, F6, has a stronger ellipticity signal than F5, while GR is stronger than both of them.

Since modified gravity distorts the size distribution of the void population, we can understand these differences by considering the ellipticity of voids as a function of size. Smaller voids are highly elliptical, since they are bounded by

irregularly-shaped walls, medium voids are more isotropic, and finally the largest voids are once again highly elliptical, since their volume-filling nature prevents them from growing uniformly in all directions (Sutter et al. 2014). The F4 model produces a significantly enhanced population of larger voids, thereby skewing the mean ellipticity.

Similar to most of the previous properties, the differences between the models become more distinct at lower redshifts. This can be caused by several factors. One potential explanation is that structure may grow faster overall in modified gravity models, enhancing differences in ellipticities over time. Another explanation is the relationship between void evolution and the screening mechanism. Although modified gravity only depends on the depth of the local Newtonian potential, rather than its gradient, the potential within a void is not uniform, and thus the effects of modified gravity can be anisotropic. As the underdensities begin to form, not every direction will empty out uniformly, leading to an anisotropic potential. Particles near the ends of the ellipse, where the potential is lowest, will become unscreened soonest, exaggerating the initial axis of expansion. However, this only applies for smaller voids as their small size will highlight any imbalances in the eigenvalues. As they expand, the ratio between the eigenvalues will begin to shrink as the modified gravity acts upon the other axes of the void. However, small voids comprise enough of the total void population to still make this a potentially observable effect.

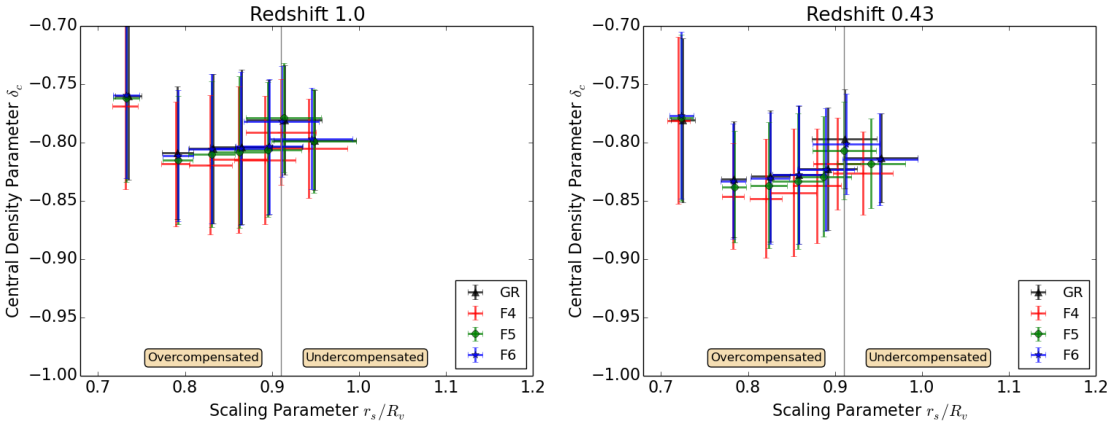

Fig. 3.4.— Best-fit values and 1σ uncertainties for the stacks of voids using the HSW profile (Hamaus et al. 2014). The thin grey line indicates the analytically-derived compensation scale. From left to right, the void stacks are of radius 10-15, 15-20, 20-25, 25-30, 30-35, 35-40, and 40-45 h^{-1}Mpc. The fits show a small but systematic trend: modified gravity acts to empty out the voids at all scales.

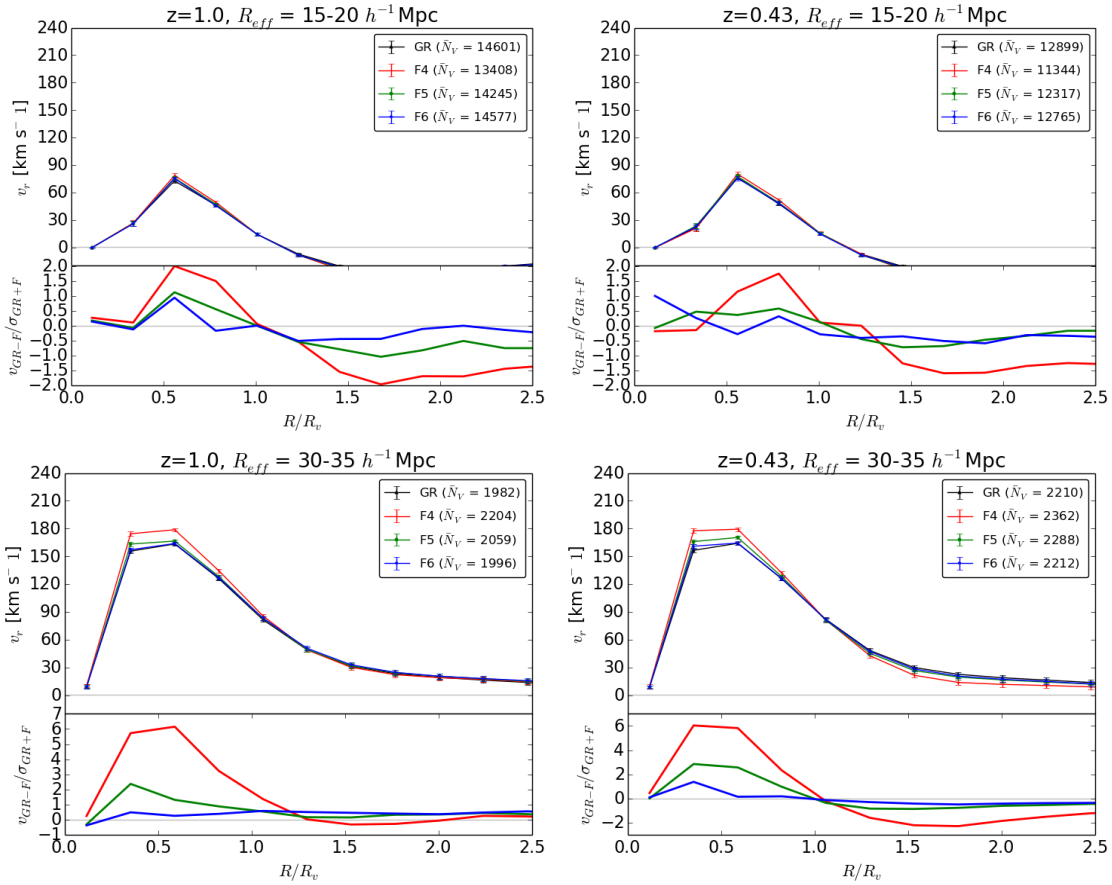

Fig. 3.5.— Mean radial velocity profiles of stacked voids with 1σ uncertainties (upper panels) and relative significance of the profiles compared to GR (lower panels). The legend in each plot indicates the mean number of voids N_v used in total to calculate profiles. The radial velocity is plotted against the relative radius, where R_v is the median void radius in each stack. Note for larger voids, the models are more easily distinguished, and there is minimal diminishing of the significance at higher redshifts. While the absolute differences between the modified gravity models and GR is larger than in the density profiles, the velocities carry greater uncertainties.

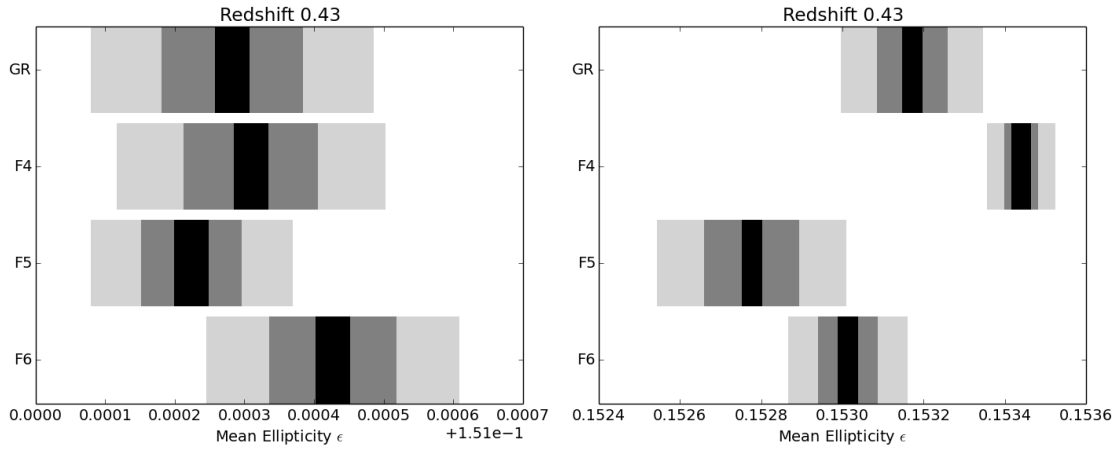

Fig. 3.6.— Mean ellipticity (black) with 1σ (dark grey) and 2σ errors on the mean for each model. All voids are used to calculate the ellipticity distributions.

Chapter 4: Void Conclusions

4.1. Trends and Comparisons with Other Studies

We have performed an initial assessment of the ability of upcoming galaxy surveys to distinguish models of modified gravity from general relativity using voids. Modifications to gravity that can be used to explain the accelerated expansion of the universe also manifest themselves as different void populations compared to general relativity. We have examined simulations including modified gravity that are designed to have identical large-scale clustering statistics as general relativity, but despite this the voids in modified gravity appear larger with steeper density profiles. The HSW profile fits show a systematic, albeit weak, impact on the profiles: voids are emptier and steeper under modified gravity. This is a direct consequence of the additional acceleration present in unscreened underdense environments. As the simulations evolve, the modified gravity has longer to operate and enhances these differences. At lower redshifts, we observe that the differences in the abundances becomes more pronounced, with the creation of even larger voids and the merging of smaller voids into larger ones.

Cai et al. (2014) have recently performed a similar analysis using a spherical-underdensity void finder. While they do observe differences in the population of small voids, our watershed technique reveals significantly more distinction populations of small voids. Indeed, most of our statistical significance derives from the small-void end of the abundance functions, whereas their main significance occurs at higher effective radii. Watershed-based void finding also appears more robust: the differences in void properties as a function of coupling strength maintain the same ordering at different sparsity levels, unlike the Cai et al. (2014) analysis. We also see more significant relative differences in the density and velocity profiles.

Finally, watershed voids are much less sensitive to galaxy bias, as shown by Sutter et al. (2014).

4.2. Survey Applicability

In the context of upcoming galaxy redshift surveys, these differences are potentially detectable. A simple Fisher forecast for $|f_{R,0}|$ using the void abundances places an upper detection limit of about 5×10^{-5}, which means that upcoming surveys may be able to rule out the F5 model. The density profiles for the low redshift survey volumes provide additional constraints, although with the low tracer density the information available only shows a roughly 2σ difference. While this does indicate a potentially detectable difference, its impact is not as large as initially suspected. The radial velocity profiles provide a large constraint, showing up to 6σ differences in both low and high redshift survey volumes. In particular with a low tracer density, the distribution of void sizes shifts to produce larger voids, in turn providing more voids that possess high outflow velocities. Of course, while the initial assessment is encouraging, radial velocity measurements possess significantly more difficult challenges and errors than measuring the positions of tracer galaxies, as the uncertainty in velocity increases with redshift and that due to the isotropic nature of voids, only roughly one in ten galaxies will be oriented in such a way as to allow for a measurement of its radial velocity. However, with the large volume of Euclid, it may be feasible to collect enough outflow velocities of voids to offset this difference in data points. Overall, the statistical significance of these profile differences falls nearly an order of magnitude below the significance found in the void abundances, which while susceptible to changes in the tracer density still appear to provide larger relative significances even when the tracer density varies by a factor of 2, a positive sign for the ability of ground based surveys examining nearer sections of the universe to detect divergences from expected GR void population statistics.

We have performed only an initial assessment, although our study includes several realistic aspects, such as sparsity and peculiar velocities. A more complete analysis would model lightcone and masking effects, and will be included in future work. It should be noted that future galaxy surveys will capture *at least* as many

voids as we have studied here. At redshift 1.0 our simulation underestimates the volume — and thus the number of voids captured — by Euclid and WFIRST. We have seen in our analysis that for detecting modified gravity there is a trade-off: higher redshifts give access to smaller statistical uncertainties, since there are more voids overall, but the modified gravity effects have not had time to largely impact void properties. It appears that these competing effects balance each other, and a space-based high-redshift survey delivers roughly comparable constraints as a ground-based low-redshift survey. Thus voids appear as a promising avenue for exploring and constraining modified gravity models that are inaccessible to traditional probes.

Chapter 5: Interferometry Pipeline Processing

While there are current indirect techniques available for reducing the impact of foreground objects (Parsons et al. 2014), techniques that have been shown to produce results that improve the sensitivity by orders of magnitude and allow for initial observations of the early structure of the universe (Parsons et al. 2012), there continue to be limitations in removing foreground objects through more direct means. One limitation arises from the need to convert the initially high resolution images observed into lower resolution images for the purposes of computing ability. With the size and resolution of current instruments, processing the images and attempting to remove foreground objects becomes intensive enough computationally that doing so at high resolution is not feasible.

We propose to develop a method that would identify high intensity areas characteristic of foreground objects and locally remove these objects using the high resolution data available. This will done through the use of NASA's Jet Propulsion Laboratory's Hierarchical Equal Area isoLatitude Pixelization (HEALPix) of a sphere (Gorski et al. 2005).

As a way of measuring the robustness of the process being designed, randomly placed objects are created and placed on an all-sky map, as seen in Figure 5.1. As a test of the process, we have been in the processing of testing the algorithm's ability to identify the peak intensity and select a large enough area to locally examine. Once the area has been selected, the high intensity area will be fitted and overlayed with a light curve which will then be subtracted from the data. Current difficulties are being faced in creating the sub-section of the all-sky map.

Once object has been identified and successfully removed while producing minimal artifacts from the process, fluctuations comparable to the fluctuations

produced by 21cm emission will be added to the all-sky map. An initial version of this can be seen in Figure 5.2. The algorithm will then be tested again to determine whether the underlying power spectrum inserted into the all-sky map to determine the degree it has been disturbed.

Once a single source has been identified and removed, multiple sources will be inserted into the all-sky map, and the algorithm will be tested again to determine its ability to accurately identify all abnormally intense objects and remove them without significantly modifying the underlying power spectrum.

Future work will continue to improve and refine by including the option to select the light curve model used to subtract out the foreground object based on the object type and eventually attempting to use the algorithm on actual collected interferometric observations and comparing the results to results obtained through the *avoidance* approach.

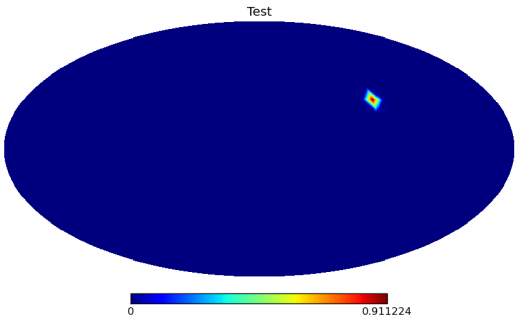

Fig. 5.1.— An all-sky map with a simulated foreground object randomly placed on it. The background level is 0.

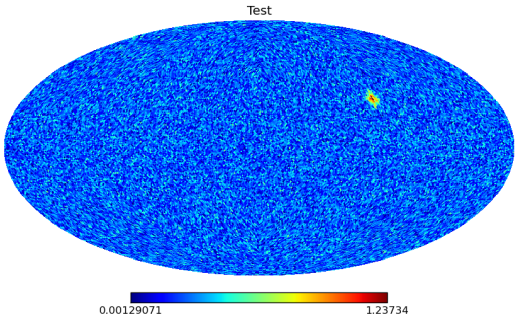

Fig. 5.2.— An all-sky map with a simulated foreground object randomly placed on it. The background level varies based on a given power spectrum that will be used to measure the impact of the subtraction technique on preserving the spectrum.

References

Abazajian K. N., et al. 2009, ApJS, 182, 543

Ahn C.P., et al. 2012, ApJS, 203, 21

Bos E. G. P., van de Weygaert R., Dolag K., Pettorino V. 2012, MNRAS, 426, 440

Cai Y.-C, Li B., Cole S., Frenk C., Neyrinck M. 2014, MNRAS, 439

Cai Y.-C, Padilla N., Li B. 2014, ArXiv e-prints: 1410.1510

Clampitt J., Cai Y.-C., Li B. 2013, MNRAS, 431, 749

Clampitt J., Jain B. 2014, ArXiv e-prints: 1404.1834

Dvali G. R., Gabadadze G., Porrati M. 2000, Phys. Rev. B, 485, 208

Fontanot F., Puchwein E., Springel V., Bianchi D. 2013, Mon. Not. R. Astron. Soc., 436

K. Gorski, E. Hivon, A. Banday, B. Wandelt, F. Hansen, et al. 2005, ApJ, 622, 759

Hamaus N., Sutter P. M., Wandelt B. D. 2014, Physical Review Letters, 112, 251302

Iliev, I. T., Shapiro, P. R., Ferrara, A., & Martel, H. 2002, ApJ, 572, L123

Ilić S., Langer M., Douspis M. 2013, Astron. & Astrophys., 556, A51

Khoury J., Weltman A. 2004, Phys. Rev. D, 69

Laureijs R., Amiaux J., Arduini S., Augueres J. ., Brinchmann J., Cole R., Cropper M., Dabin C., Duvet L., Ealet A., et al. 2011, ArXiv:1110.3193

Lavaux G., Wandelt B. D. 2012, ApJ, 754, 109

Levi M., Bebek C., Beers T., Blum R., Cahn R., Eisenstein D., Flaugher B., Honscheid K., Kron R., Lahav O., McDonald P., Roe N., Schlegel D., representing the DESI collaboration 2013, ArXiv e-prints: 1308.0847

Li B., Zhao G.-B., Koyama K. 2012, Mon. Not. R. Astron. Soc., 421, 3481

Lonsdale, C. J., Cappallo, R. J., Morales, M. F., et al. 2009, IEEE Proceedings, 97, 1497

Maartens R., 2004, Living Reviews in Relativity, 7

Melchior P., Sutter P., Sheldon E., Krause E., Wandelt B. 2014, Mon. Not. R. Astron. Soc., 440

Neyrinck M. C., 2008, Mon. Not. R. Astron. Soc., 386, 2101

Pan D. C., Vogeley M. S., Hoyle F., Choi Y.-Y., Park C. 2012, Mon. Not. R. Astron. Soc., 421, 926

Parsons, A. R., Pober, J. C., Aguirre, J. E., et al. 2012b, ApJ, 756, 165

Parsons, A. R., Liu, A., Aguirre, J. E., et al. 2014, ApJ, 788, 106

Pisani A., Lavaux G., Sutter P. M., Wandelt B. D. 2014, Mon. Not. R. Astron. Soc., 443, 3238

Pisani A., Sutter P. M., Wandelt B. D., 2014, (in prep)

Planck Collaboration Ade P. A. R., Aghanim N., Armitage-Caplan C., Arnaud M., Ashdown M., Atrio-Barandela F., Aumont J., Baccigalupi C., Banday A. J., et al. 2014b, Astron. & Astrophys., 571, A19

Planck Collaboration Ade P. A. R., Aghanim N., Armitage-Caplan C., Arnaud M., Ashdown M., Atrio-Barandela F., Au- mont J., Baccigalupi C., Banday A. J., et al. 2014a, Astron. & Astrophys., 571, A16

Platen E., van de Weygaert R., Jones B. J. T. 2007, Mon. Not. R. Astron. Soc., 380, 551

Reid B. A., et al. 2012, Mon. Not. R. Astron. Soc., 426, 2719

Shim J., Lee J., Li B. 2014, Astrophys. J., 784

Spergel D., et al. 2013, ArXiv e-prints: 1305.5422

Sutter P. M., Carlesi E., Wandelt B. D., Knebe A. 2015, Mon. Not. R. Astron. Soc., 446, L1

Sutter P. M., Lavaux G., Hamaus N., Pisani A., Wandelt B. D., Warren M., Villaescusa-Navarro F., Zivick P., Mao Q., Thompson B. B. 2015, Astronomy and Computing, 9, 1

Sutter P. M., Lavaux G., Hamaus N., Wandelt B. D., Weinberg D. H., Warren M. S. 2014, Mon. Not. R. Astron. Soc., 442, 462

Sutter P. M., Lavaux G., Wandelt B. D., Weinberg D. H. 2012a, ApJ, 761, 187

Sutter P.M., Lavaux G., Wandelt B. D., Weinberg D. H. 2012b, ApJ, 761, 44

Sutter P.M., Lavaux G.,Wandelt B. D.,Weinberg D. H.,Warren M. S., Pisani A. 2014, Mon. Not. R. Astron. Soc., 442, 3127

Sutter P. M., Pisani A., Wandelt B. D., Weinberg D. H. 2014, Mon. Not. R. Astron. Soc., 443, 2983

van Haarlem, M. P., Wise, M. W., Gunst, A. W., et al. 2013, A& A, 556, A2

Zhao B., Li B., Koyama K., 2011, Phys. Rev. D, 83